JOURNAL OF THERMOPHYSICS AND HEAT TRANSFER
Vol. 18, No. 4, October–December 2004

Flow and Heat-Transfer Computations in Rotating Rectangular Channels with V-Shaped Ribs

Guoguang Su,* Shuye Teng,* Hamn-Ching Chen,† and Je-Chin Han‡
Texas A&M University, College Station, Texas 77843

Computations were performed to study three-dimensional turbulent flow and heat transfer in a rotating rectangular channel with V-shaped ribs. The channel aspect ratio is 4:1, the rib-height-to-hydraulic-diameter ratio e/D_h is 0.078, and the rib-pitch-to-height ratio P/e is 10. A total of eight calculations have been performed with various combinations of rotation number, Reynolds number, coolant-to-wall density ratio, and channel orientation. The rotation number and inlet coolant-to-wall density ratio were varied from 0.0 to 0.28 and from 0.122 to 0.40, respectively, whereas the Reynolds number was varied from 10^4 to 5×10^5. Three channel orientations (90, −135, and 135 deg from the rotation direction) were also investigated. A multiblock Reynolds-averaged Navier–Stokes method was employed in conjunction with a near-wall second-moment turbulence closure for detailed predictions of the mean velocities, mean temperature, turbulent Reynolds stresses, and heat fluxes.

Nomenclature

AR	=	channel aspect ratio
D_h	=	hydraulic diameter, m
e	=	rib height, m
h	=	heat-transfer coefficient, $q_w/(T_w - T_b)$, w/(m$^2 \cdot$ °C)
k	=	thermal conductivity of coolant, w/(m $\cdot$ °C)
L	=	total length of the channel, m
L_1	=	unheated smooth starting section of the channel, m
L_2	=	heated ribbed section of the channel, m
L_3	=	unheated smooth exit section of the channel, m
Nu	=	local Nusselt number, hD_h/k
Nu_0	=	Nusselt number in fully developed turbulent nonrotating tube flow
Pr	=	Prandtl number
Re	=	Reynolds number, $W_b D_h/\nu$
Ro	=	rotation number, $\Omega D_h/W_b$
R_r	=	radius from axis of rotation, m
S	=	streamwise distance, m
T	=	local coolant temperature, °C
T_b	=	bulk mean temperature, °C
T_w	=	local wall temperature, °C
T_0	=	coolant temperature at inlet, °C
W_b	=	bulk velocity in streamwise direction, volume flow rate/area, m/s
α	=	rib angle
β	=	channel orientation measured from direction of rotation
$\Delta\rho/\rho$	=	inlet coolant-to-wall density ratio, $(T_w - T_0)/T_w$
θ	=	dimensionless temperature, $(T - T_0)/(T_w - T_0)$
ν	=	kinematic viscosity of coolant, m^2/s
ρ	=	density of coolant, kg/m^3
Ω	=	rotational speed, rad/s

Introduction

GAS-TURBINE stages are being designed to operate at increasingly higher inlet temperatures to improve thermal efficiencies. Sophisticated cooling techniques must be employed to cool the components to maintain the performance requirements. A widely used method for cooling turbine blades is to bleed lower-temperature air from the compressor and circulate it within and around each blade. The coolant typically flows through a series of straight ducts connected by 180-deg turns and roughened with ribs or pin fins to enhance heat transfer. These cooling ducts might not only be square in cross section or normal to the rotational direction of the blade. In fact, the aerodynamic shape of the turbine blade dictates the use of cooling channels that are rectangular in cross section (with different aspect ratios) and are at an angle β other than 90 deg from the direction of rotation. Rotation of the turbine blade cooling passages adds another complexity to the problem. It gives rise to Coriolis and buoyancy forces that can significantly alter the local heat transfer in the internal coolant passages from the nonrotating channels. The presence of rib turbulators adds a further complexity because these ribs produce complex flowfields such as flow separation, reattachment, and secondary flow between the ribs, which produce a high turbulence level that leads to high heat-transfer coefficients. The complex coupling of the Coriolis and buoyancy forces with flow separation/reattachment by ribs has prompted many investigators to study, both experimentally and numerically, the flow and temperature fields generated in heated rotating ribbed wall passages.

Several studies have been made to predict numerically the flow and heat transfer in rotating smooth and ribbed ducts. Stephens et al.[1,2] studied inclined ribs in a straight nonrotating square duct. Lin et al.[3] investigated the effect of angled ribs on the heat-transfer coefficients in a rotating two-passage duct using a shear-stress-transport turbulence model. They studied the effects of Reynolds numbers, rotation numbers, and buoyancy parameters. Prakash and Zerkle[4] employing a high-Reynolds-number k–ε turbulence model with wall function, performed a numerical prediction of flow and heat transfer in a rectangular duct with 90-deg ribs with and without rotation. However, their calculations used periodicity and neglected buoyancy effects. They suggested that a low-Reynolds-number turbulence model is necessary to simulate real-gas turbine engine conditions and a Reynolds-stress model is required to capture anisotropic effects. Bonhoff et al.[5] calculated the heat-transfer coefficients and flowfields for rotating U-shaped coolant channels with 45-deg angled ribs. They used a Reynolds-stress turbulence model with wall functions in the FLUENT computational-fluid-dynamics (CFD) code. Using the periodicity of the flow, Iacovides[6] computed flow and temperature fields in a rotating straight duct with 90-deg ribs. Two zonal models of turbulence were tested: a k–ε with a one-equation model of k transport across the near-wall region and a low-Reynolds-number differential stress model. He concluded that the differential stress model thermal computations were clearly superior to those of the k–ε/one-equation model.

Received 5 March 2004; revision received 8 May 2004; accepted for publication 10 May 2004.

*Research Assistant, Turbine Heat Transfer Laboratory, Department of Mechanical Engineering.

†Professor, Ocean Engineering Program, Department of Civil Engineering. Senior Member AIAA.

‡M. C. Easterling Chair, Turbine Heat Transfer Laboratory, Department of Mechanical Engineering. Associate Fellow AIAA.

Using the same model and method of Chen et al.,[7,8] Jang et al.[9,10] studied flow and heat-transfer behavior in a nonrotating two-pass square channels with 60- and 90-deg ribs, respectively. Their results were in good agreement with Ekkad and Han's[11] detailed heat-transfer data and demonstrated the second-moment closure model superiority in predicting flow and heat-transfer characteristics in the ribbed duct. In a later study, Jang et al.[12] predicted flow and heat transfer in a rotating square channel with 45-deg angled ribs by the same second-moment closure model. Heat-transfer coefficient prediction matched very well with the data obtained by Johnson et al.[13] for both stationary and rotating cases. Al-Qahtani et al.[14] predicted flow and heat transfer in a rotating two-pass rectangular channel ($AR = 4{:}1$) with 45-deg angled ribs using the same second-moment closure model of Chen et al.[7,8] Their heat-transfer coefficient prediction was compared with the data of Azad et al.[15] for both stationary and rotating cases. Their study predicted fairly well the complex three-dimensional flow and heat-transfer characteristics resulting from angled ribs, sharp 180-deg turn, rotation, centrifugal buoyancy forces, and channel orientation. Al Qahtani et al.[16] also conducted a numerical study of flow and heat transfer in one-pass rotating rectangular channels ($AR = 4{:}1$) with 45-deg rib turbulators using the same second-moment closure model. Their flow and heat-transfer predictions were in good agreement with the experimental data of Griffith et al.[17] Using a Reynolds-stress turbulence model, Jia et al.[18] predicted local heat-transfer and fluid flow characteristics in straight stationary square ducts with transverse and V-shaped ribs for Reynolds number from 1.4×10^4 to 3.5×10^4. They concluded that V-shaped ribs pointing upstream performed superior to V-shaped ribs pointing downstream and transverse ribs.

In addition to the numerical studies just mentioned, there were several experimental studies focused on internal cooling passages in nonrotating ducts, such as Han and Park,[19] Han et al.,[20] Ekkad and Han,[11] and Liou et al.[21] Experimental studies on rotating ducts have been less numerous. Wagner et al.,[22] Dutta and Han,[23] Soong et al.,[24] and Azad et al.[15] investigated rotating ducts with smooth and ribbed walls. Wagner et al.,[25] Johnson et al.,[13,26] Parsons et al.,[27] and Zhang et al.[28] reported studies on rotating square channels with normal and angled ribs. Azad et al.[15] also investigated the effect of channel orientation on rotating ribbed two-pass rectangular channel. Griffith et al.[17] studied the effect of channel orientation on rotating smooth and ribbed rectangular channels with channel aspect ratio of 4:1. They investigated a broad range of flow parameters including Reynolds number ($Re = 5 \times 10^3 - 4 \times 10^4$), rotation number ($Ro = 0.04 - 0.3$), and coolant-to-wall density ratio ($\Delta\rho/\rho = 0.122$).

The present study is concerned specifically with the numerical prediction of flow and heat transfer in rectangular channels with V-shaped ribs. Several experimental studies have been conducted to investigate the heat-transfer enhancement in square and rectangular channels with V-shaped ribs. Han et al.[20] found that the 60- and 45-deg V-shaped ribs perform better than the 60- and 45-deg parallel angled ribs in square channels. Ekkad and Han[11] also showed that the nonrotating square channel with 60-deg V-shaped rib produced more heat-transfer enhancement than 60- and 90-deg angled ribbed channels. Al-Hadhrami and Han[29] and Al-Hadhrami et al.[30] studied the effect of rotation on heat transfer in rotating two-pass square and rectangular channels ($AR = 2{:}1$) with rib turbulators for five different channel orientations. They found that the parallel and V-shaped ribs produced better heat-transfer enhancement than the crossed and inverted V-shaped ribs. Lee et al.[31] studied the heat transfer in rotating rectangular channels ($AR = 4{:}1$) with V-shaped and angled rib turbulators with and without gaps. They concluded that the V-shaped ribs produced more heat-transfer enhancement than the angled ribs for both the stationary and rotating cases, and the enhancement on both the leading and trailing surfaces increases with rotation. The experimental results of Lee et al.[31] for narrow rectangular channels ($AR = 4{:}1$) with V-shaped ribs provided a validation database for the present work.

The preceding experimental studies show that V-shaped ribs produce overall better heat-transfer enhancement than the angled ribs. However, the effects of rotation, channel orientation, and large channel aspect ratio on the secondary flow and heat-transfer calculations in rectangular channels with V-shaped ribs have not been systematically investigated in previous numerical studies. Furthermore, there is no reported information on the flow and heat-transfer behaviors in stationary/rotating rectangular channels with V-shaped ribs under very high-Reynolds-number flow conditions ($Re \sim 5 \times 10^5$). The objective of this study is to use the second-moment Reynolds-averaged Navier–Stokes (RANS) method of Chen et al.[7,8] 1) to predict the three-dimensional flow and heat transfer for rotating one-pass rectangular ducts ($AR = 4{:}1$) with V-shaped ribs and compare with the experimental data of Lee et al.[31] and 2) to investigate the effect of high rotation number, high Reynolds number, and high density ratio on the secondary flowfield and the heat-transfer characteristics in a rectangular duct with V-shaped ribs rotating at −135-, 90-, and 135-deg orientation.

Description of Problem

A schematic diagram of the geometry is shown in Fig. 1. The channel has a rectangular cross section with a channel aspect ratio AR of 4:1. Of the four side walls, the two in the rotational direction are denoted as leading and trailing surfaces, whereas the other two are denoted as top and bottom surfaces. The channel hydraulic diameter D_h is 0.8 in. (2.03 cm). The distance from the inlet of the channel to the axis of rotation is given by $R_r/D_h = 20.0$. The total length of the channel L equals to $22.5D_h$. The channel consists of an unheated smooth starting section ($L_1/D_h = 9.92$), a heated ribbed section ($L_2/D_h = 7.58$), and an unheated smooth exit section ($L_3/D_h = 5.00$). In the ribbed section, as shown in Fig. 1, the leading and trailing surfaces are roughened by nine equally spaced 45-deg V-shaped ribs with square cross section. The in-line V-shaped ribs are parallel and point upstream. The rib height-to-hydraulic diameter ratio e/D_h is 0.078. The rib pitch-to-height ratio P/e is 10. Three channel orientations ($\beta = 90$ deg, $\beta = -135$ deg, $\beta = 135$ deg) are studied, with $\beta = 90$ deg corresponding to the midportion and $\beta = -135$ and 135 deg to the trailing-edge region of a blade. A summary of all eight cases studied is given in Table 1.

Computational Procedure

Overview

The RANS equations in conjunction with a near-wall Reynolds-stress turbulence model are solved using the chimera RANS method of Chen et al.[7,8] The governing equations with the second-moment closure turbulence model were described in detail in Chen et al.[7,8] and will not be repeated here. The flow is considered to be incompressible because the Mach number is quite low. However, the density in the centrifugal force terms is approximated by $\rho = \rho_0 T_0/T$ to account for the density variations caused by the temperature differences. ρ_0 and T_0 are the density and temperature at the inlet of the cooling channel. In general, the density is also a function of the rotating speed because the centrifugal force creates a pressure gradient along the duct. In the experiments of Lee et al.,[31] the maximum pressure variation between the channel inlet and the exit is approximately 0.0113 atm for the highest rotation number of 0.28 considered in the present study. This gives a maximum density variation of only about 1.1% from the inlet to the exit of the duct at the highest rotation number. It is therefore reasonable to omit the density variation caused by the pressure gradients induced by the channel rotation.

Table 1 Summary of cases studied

Case No.	Ro	$\Delta\rho/\rho$	β, deg	Re
1	0.00	0.122	——	10^4
2	0.14	0.122	90	10^4
3	0.14	0.122	135	10^4
4	0.14	0.122	−135	10^4
5	0.00	0.122	——	10^5
6	0.00	0.122	——	5×10^5
7	0.28	0.200	135	5×10^5
8	0.28	0.400	135	5×10^5

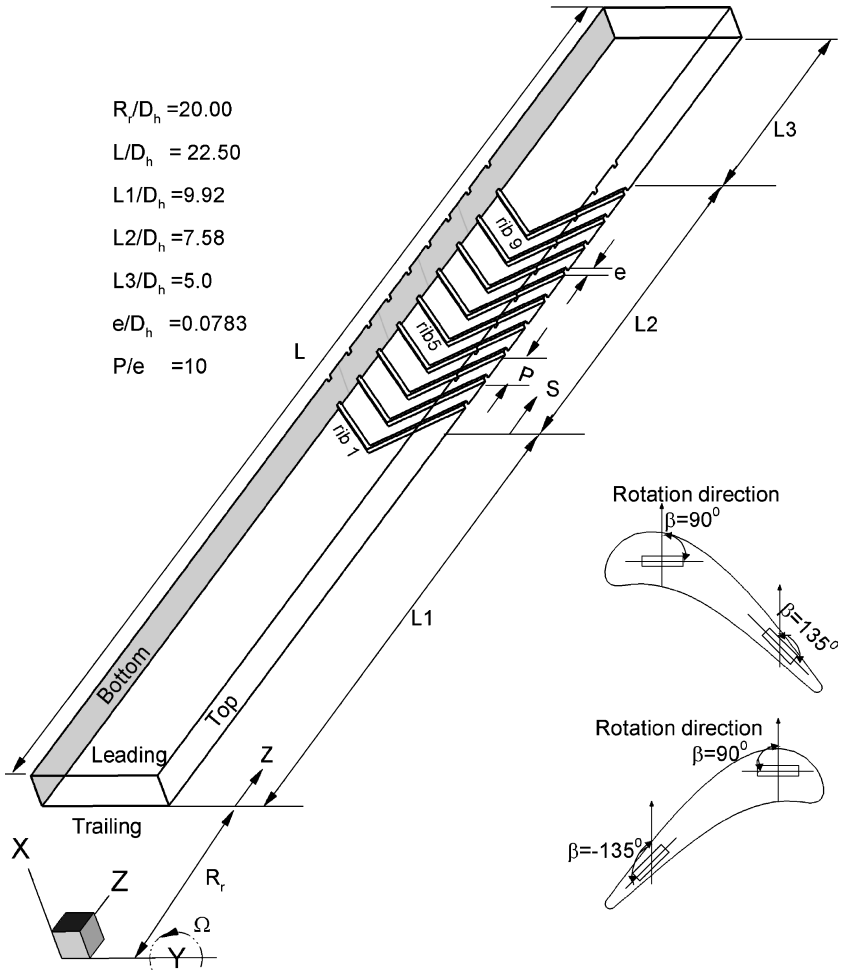

Fig. 1 Geometry and conceptual view of rotating channel orientation for rectangular duct (AR = 4:1) with in-line V-shaped ribs on leading and trailing surface.

Boundary Conditions

A uniform velocity profile was used at the inlet of the duct ($Z = 0$). The unheated length L_1 was long enough for the velocity profile to be fully developed turbulent profile before the heating start point ($Z = L_1$). At the exit of the duct, zero-gradient boundary conditions were specified for the mean velocity and all turbulent quantities, whereas linear extrapolation was used for the pressure field. The coolant fluid at the inlet of the duct is air at uniform temperature $T = T_0$ [i.e., $\theta = (T - T_0)/(T_w - T_0) = 0$]. The wall temperature of the unheated sections is kept constant at $T = T_0(\theta = 0)$, whereas the wall temperature of the heated section is kept constant at $T = T_w(\theta = 1)$.

Computational Grid Details

Figure 2a shows the computational grid around the ribs for the ribbed duct. The grid was generated using an interactive grid-generation code GRIDGEN.[32] It was then divided into five overlapped chimera grid blocks (three for the case of smooth duct) to facilitate the implementation of the near-wall turbulence model and the specification of the boundary conditions. To provide adequate resolutions of the viscous sublayer and buffer layer adjacent to a solid surface, the minimum grid spacing for the $Re = 10^4$ cases is maintained at 10^{-3} of the hydraulic diameter, which corresponds to a wall coordinate y^+ of the order of 0.3; the minimum grid spacing for the $Re = 5 \times 10^5$ cases is maintained at 2×10^{-5} of the hydraulic diameter, which corresponds to wall coordinate y^+ of the order of 0.3. The number of grid points in the streamwise direction is 402 (with 373 in the ribbed section), and the number of grid points in the cross-stream plane is 43×75 for $Re = 10^4$ cases. For the high-Reynolds-number ($Re = 10^5$ and 5×10^5) cases, the number of grid points in the cross-stream plane was increased from 33×75 to 43×85, whereas the number of grid points in the streamwise direction was maintained at 373 for the ribbed section. It is clearly seen from the grid-refinement studies shown in Figs. 2b and 2c that these grid distributions produced nearly grid-independent solutions for the $Re = 10^4$ and 5×10^5 cases, respectively. In all calculations, the rms and maximum absolute errors for both the mean flow and turbulence quantities were monitored for each computational block to ensure complete convergence of the numerical solutions, and a convergence criterion of 10^{-5} was used for the maximum rms error.

Results and Discussion

Velocity and Temperature Fields

As summarized in Table 1, computations were performed with Reynolds numbers Re ranging from 10^4 to 5×10^5, rotation number Ro from 0 to 0.28, inlet coolant-to wall density ratio $\Delta\rho/\rho$ from 0.122 to 0.4, and channel orientations from −135 deg to 90 deg to 135 deg. The Nusselt numbers presented here are normalized with a smooth tube correlation by Dittus–Boelter for fully developed turbulent nonrotating tube flow:

$$Nu_0 = 0.023 Re^{0.8} Pr^{0.4} \tag{1}$$

Figure 3 shows the velocity vector field and dimensionless temperature contour θ near the ribbed surface for the nonrotating case (case 1) listed in Table 1. As we can see from the figure, because the ribs are oriented at a 45-deg angle pointing upstream the fluid in the center of the channel reaches the ribs first and moves along the ribbed surfaces toward the side walls, that is, the top and bottom

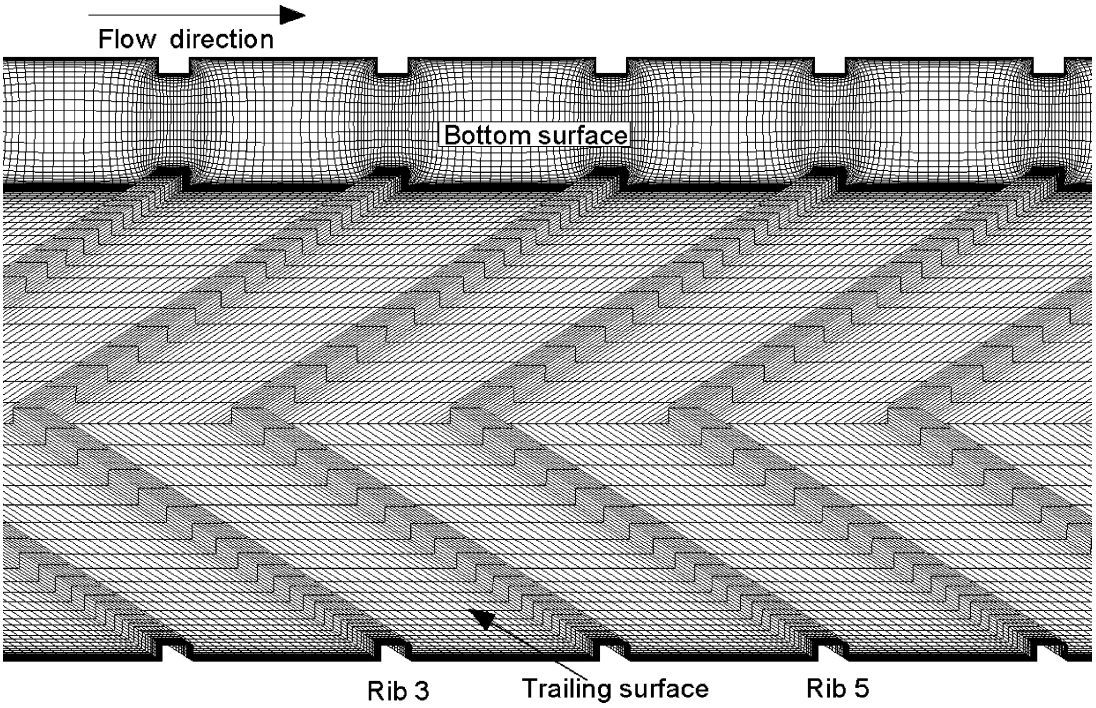

Fig. 2a Numerical grid.

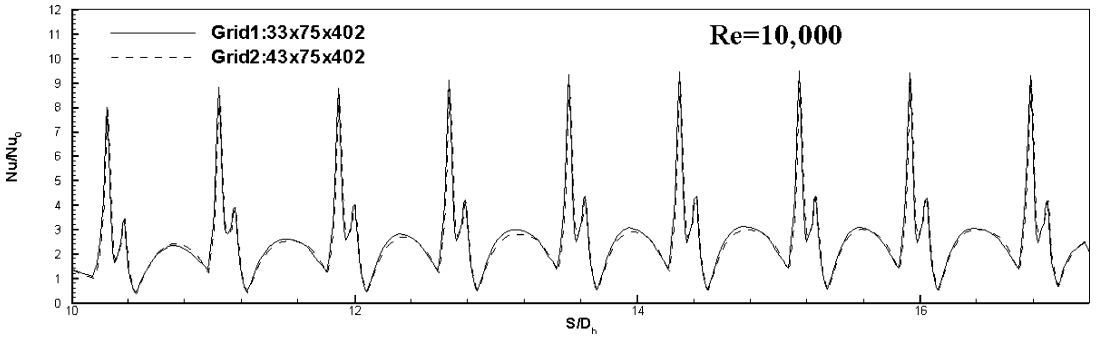

Fig. 2b Grid-refinement study for $Re = 10^4$.

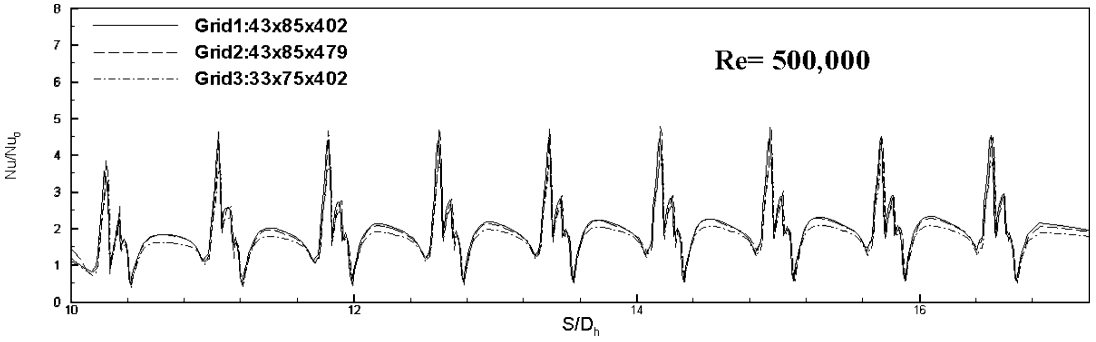

Fig. 2c Grid-refinement study for $Re = 5 \times 10^5$.

surfaces. It is also observed that the ribs produce repeated flow separations and reattachment in the streamwise direction. The cooler fluid impingement induced by the V-shaped ribs leaves behind each rib a V-shaped temperature contour. This dimensionless temperature contour is closely related to the streamwise velocity and secondary flow patterns induced by the V-shaped ribs. The temperature is high immediately downstream of each rib because of flow separations behind the ribs. In the middle section between the ribs, however, the temperature is relatively low as a result of the impingement of cooler fluids in the flow reattachment zone. As the coolant flow near the ribbed surface is directed towards the side walls by the ribs, the value level of the V-shaped temperature contour increases, that is, the coolant gets hotter, in the direction of the inclined ribs.

Figure 4 shows the secondary flow vectors and dimensionless temperature contours both on top of and between several selected V-shaped ribs for case 1. The secondary flow vectors show that the V-shaped ribs produce very strong tangential velocities which carry the cooler fluid from the center of the channel towards the side walls. The flow on top of the ribs is nearly parallel to the ribbed surface, and its vertical velocity components are rather weak. The

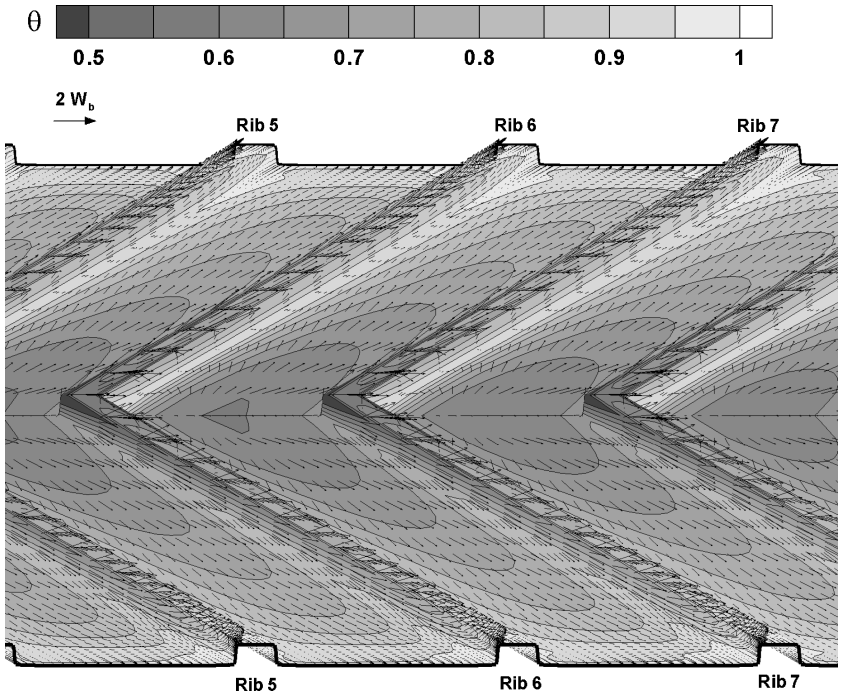

Fig. 3 Velocity vectors and dimensionless temperature θ contours close to the rib surface for nonrotating duct ($Re = 10^4$, $Ro = 0.0$, $\Delta\rho/\rho = 0.122$).

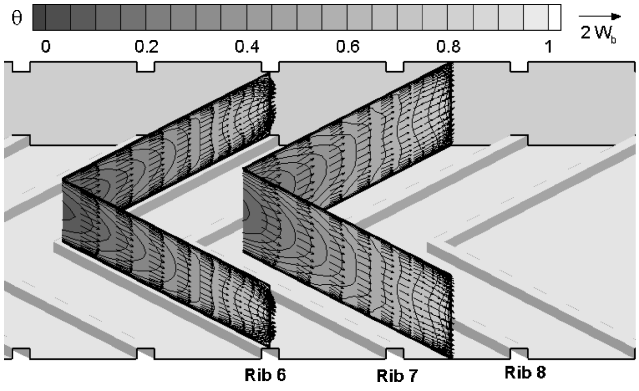

a) Tangential velocity vectors

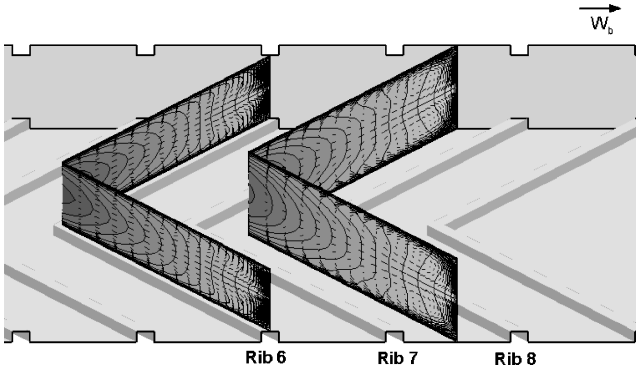

b) Secondary flow vectors

Fig. 4 Tangential velocity and secondary flow vectors and dimensionless temperature θ contours on and between ribs for nonrotating duct ($Re = 10^4$, $Ro = 0.0$, $\Delta\rho/\rho = 0.122$).

vertical velocity components of the flow behind ribs are significantly stronger because of flow reattachment (impingement) between ribs. Also observed from Fig. 4 is the early stage development of two pairs of counter-rotating vortices on top of each rib, which grow into four full symmetric counter-rotating vortices in the midsection between ribs.

Figure 5 gives the calculated dimensionless temperature contours near the ribbed surface and at selected cross sections for the nonrotating case (case 1). As it is shown on the symmetric plane along the channel centerline, coolant temperature increases in the streamwise direction as the coolant flows down the channel and is heated by the channel walls. The temperature contours near the ribbed surfaces show small areas of low temperature on the front edge of the ribs, indicating coolant impingement on the ribs. High temperatures right behind ribs indicate flow separation. Relatively lower temperatures between ribs indicate coolant impingement and reattachment. Temperature contours between two ribs expand in the 45-deg angle from the center plane, indicating that the coolant near the ribbed surface is flowing along the 45-deg inclined ribs from the center of the channel to the side walls. The temperature contours on the cross sections cut in the direction of the inclined ribs show that the temperature is relatively low near the center of the channel, but increases gradually towards the side walls in the direction of the V-shaped ribs as the coolant flows along the inclined ribs. Similar temperature contour patterns are observed between and above ribs. However, as coolant flows down the channel, the temperature gradient in the spanwise direction is gradually weakened as a result of the continuous heating of the coolant by the wall.

Figure 6 shows velocity vectors and temperature contours on two selected planes in a rotating duct (case 2). These two planes are parallel to the mainstream direction and perpendicular to the leading and trailing surfaces. Plane 1 spans over ribs 7 and 8, whereas plane 2 spans over ribs 4 and 5. The distance between plane 1 and the bottom surface is $1.25D_h$ and that between plane 2 and the top surface is $0.31D_h$. Velocity vectors in planes 1 and 2 indicate that there is flow separation right behind each rib, and flow reattachment (impingement) happens in the middle section between every two neighboring ribs. Because of duct rotation and Coriolis force effect

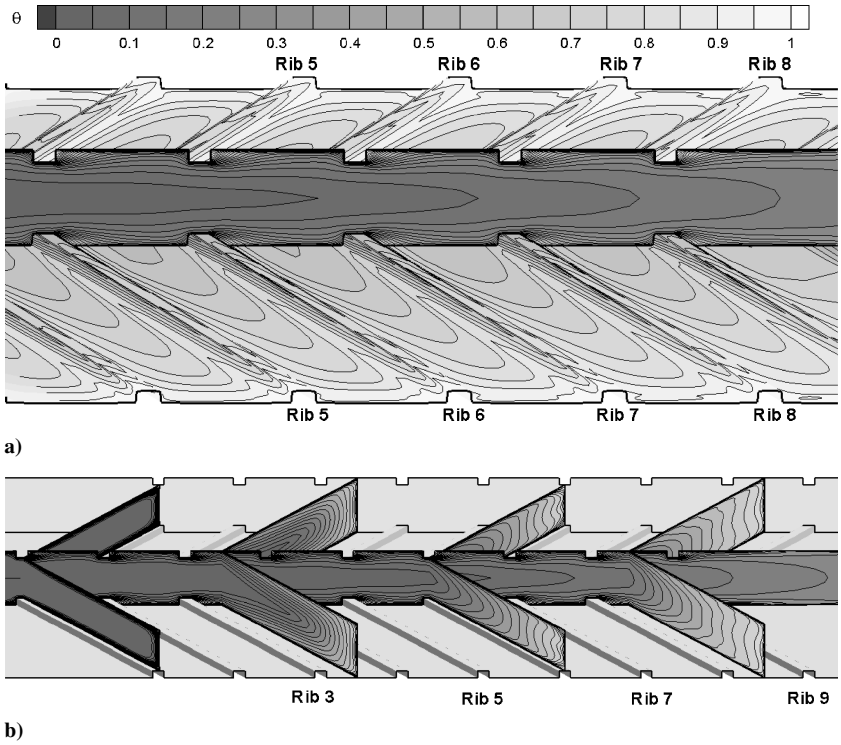

Fig. 5 Dimensionless temperature θ contours for nonrotating ducts: a) close to the rib surface and along the center plane of symmetry; b) selected cross sections ($Re = 10^4$, $Ro = 0.0$, $\Delta\rho/\rho = 0.122$).

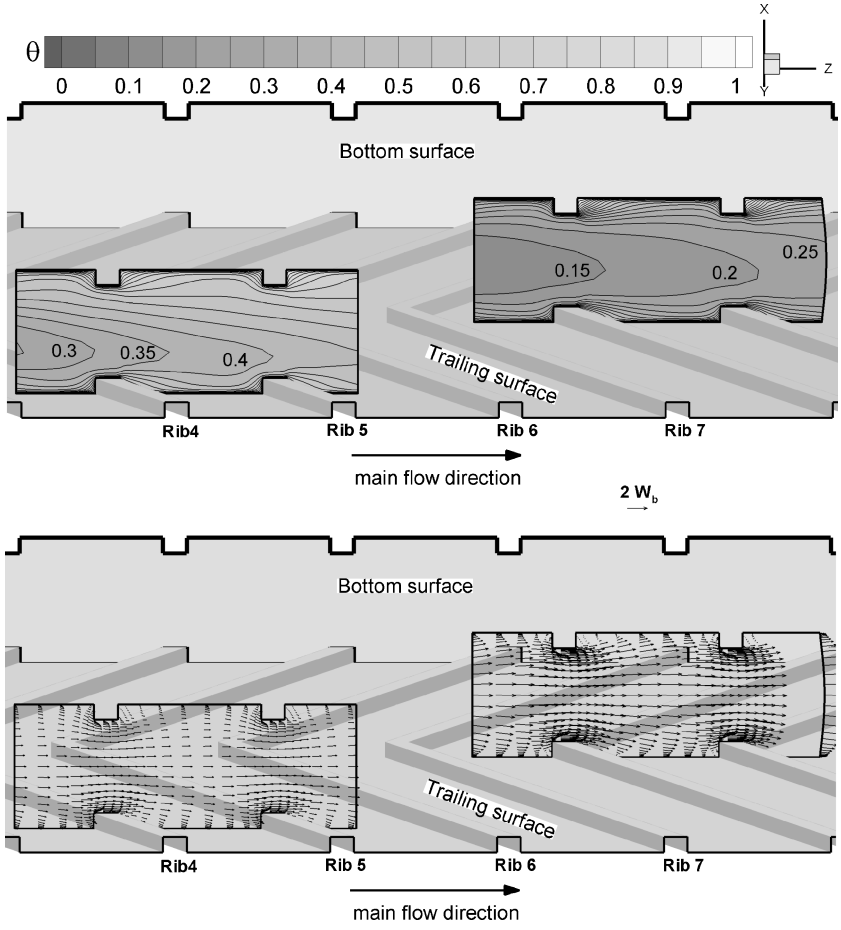

Fig. 6 Flow along mainstream direction and dimensionless temperature θ contours for rotating duct ($Re = 10^4$, $\Delta\rho/\rho = 0.122$, $Ro = 0.14$, $\beta = 90$ deg).

(relatively small rotation effect at $Ro = 0.14$), velocity vectors in plane 1 are slightly distorted toward the trailing surface as compared to the nonrotating case 1. This flow distortion is even more obvious in plane 2 because it is farther away from the center of the channel. Temperature contours on both planes are affected accordingly. The coolant flow is pushed towards the trailing surface by the Coriolis force, causing the temperature on the leading side to be higher than that on the trailing side. It is also observed from Fig. 6 that the low-temperature core of the coolant flow shrinks significantly in the spanwise direction as the fluid flows down the duct. Although plane 1 spans over two ribs downstream of plane 2, the temperatures of plane 1 are much lower than those of plane 2 because plane 2 is much closer to the side wall.

To provide a more detailed understanding on the heat-transfer enhancement caused by V-shaped ribs, it is worthwhile to examine the secondary flow vectors and temperature contours along the ribbed channel in the manner shown in Figs. 7–9. Figures 7–9 provide the secondary flow and dimensionless temperature contours at selected cross sections for cases 1, 2, and 3. The channel orientation is 90 deg in case 2 and 135 deg in case 3. Both cases 2 and 3 have a rotating number of 0.14.

As shown in Fig. 7, in the smooth section before the first rib four pairs of corner vortices are generated as a result of the Reynolds-stress anisotropy. As the flow approaches the V-shaped ribs, these corner vortices are overpowered by two new pairs of V-shaped rib-induced vortices. The strength of these four rib-induced vortices increases considerably in the middle section between two ribs. The size of these four counter-rotating vortices oscillates along the streamwise direction from the largest in the middle of each interrib distance to the smallest on the rib tops. This pattern of oscillation repeats itself until the end of the last rib. The effect of this secondary flow on the temperature field is that the cooler fluid in the core region is convected along the ribbed surface to the top and bottom surfaces, that is, the side walls. This results in steep temperature gradients and high heat-transfer coefficients on the ribbed surfaces as seen in the corresponding temperature contours.

Figure 8 shows that the Coriolis force produces in front of the first rib a cross-stream two-vortex flow structure. The two vortexes are symmetric along the x axis. As the flow approaches the rib, the secondary flow induced by the Coriolis force starts to distort the secondary flow induced by the V-shaped rib. A comparison between Figs. 7 and 8 shows that 1) the magnitude of the secondary flow

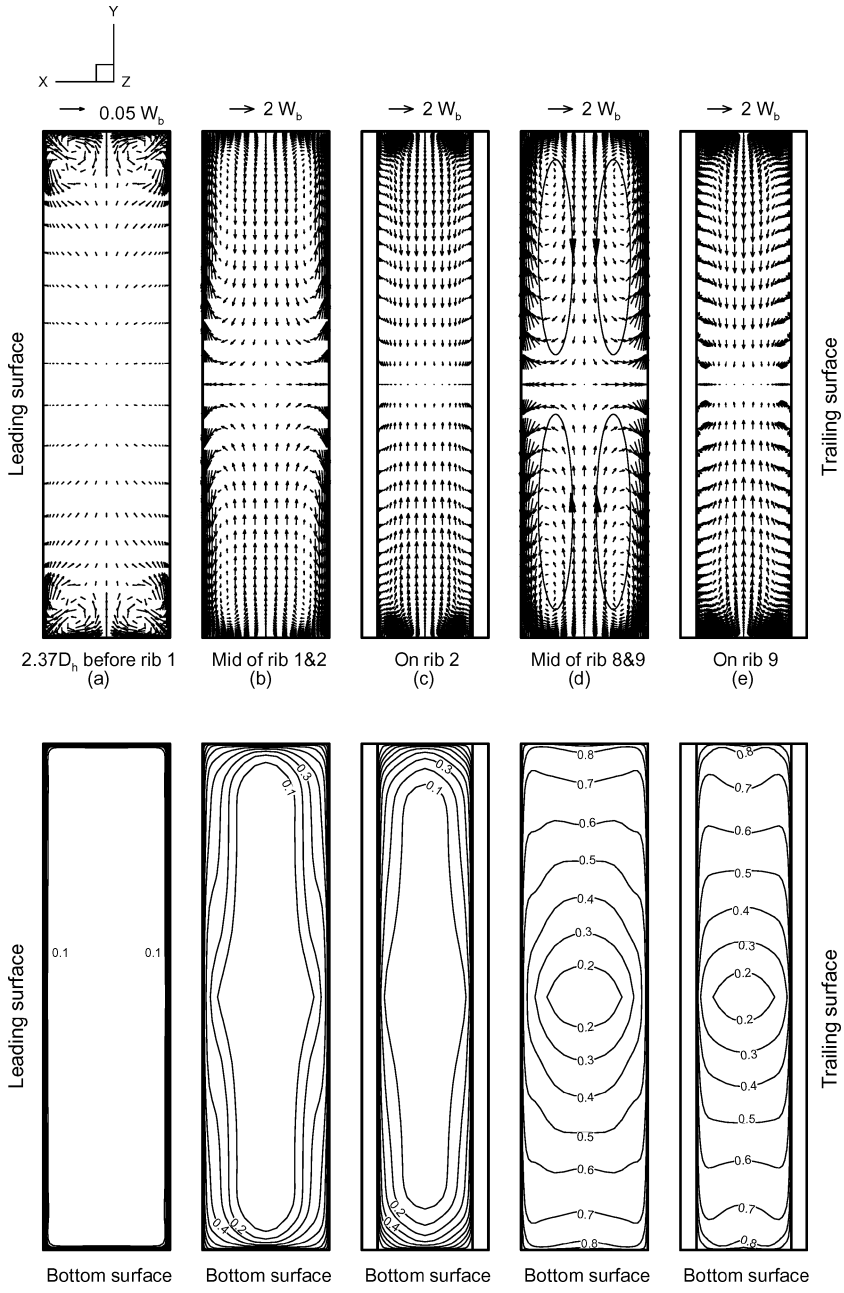

Fig. 7 Secondary flow and dimensionless temperature θ contours for nonrotating duct ($Re = 10^4$, $Ro = 0.0$, $\Delta\rho/\rho = 0.122$).

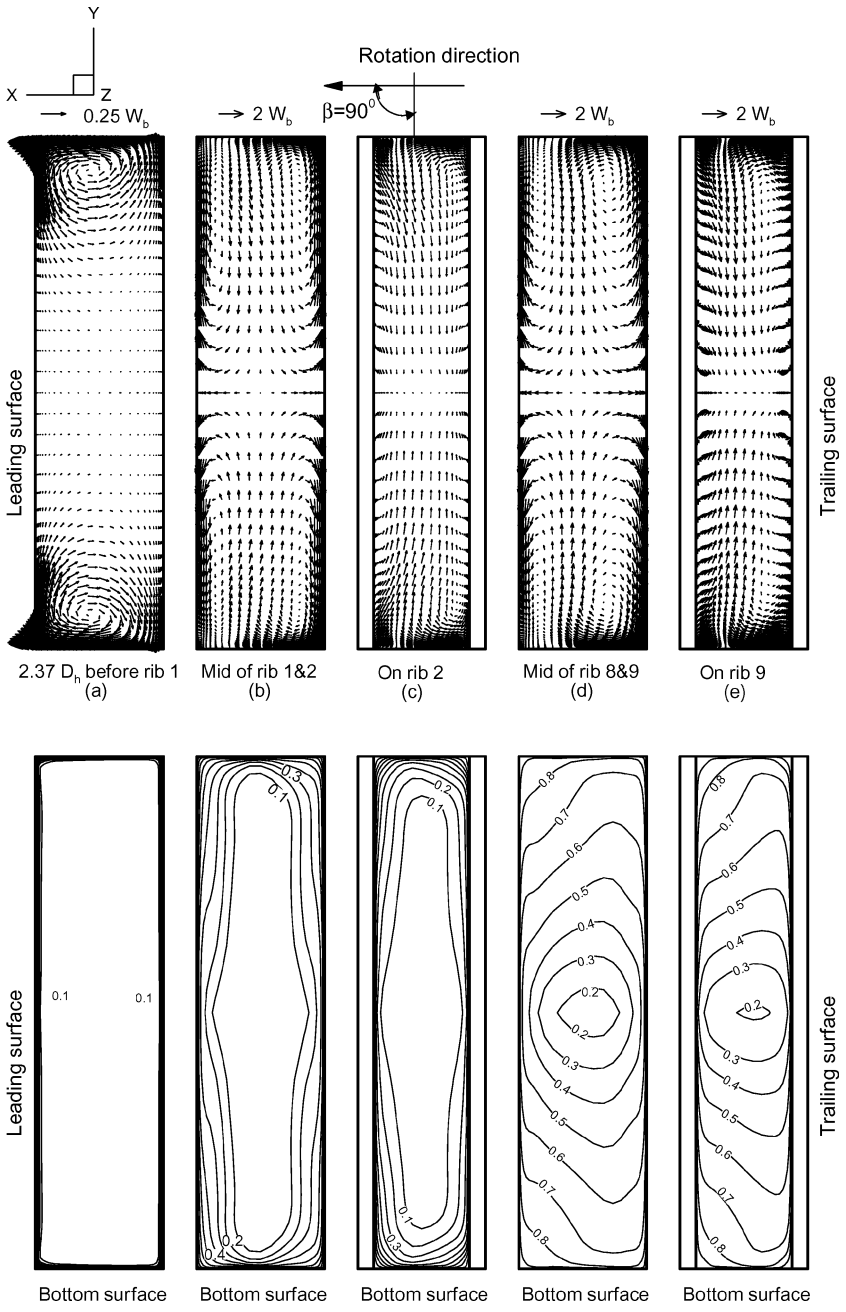

Fig. 8 Secondary flow and dimensionless temperature θ contours for rotating duct ($Re = 10^4$, $\Delta\rho/\rho = 0.122$, $Ro = 0.14$, $\beta = 90$ deg).

induced by the Coriolis force is weaker than that induced by the V-shaped rib; 2) because of the Coriolis force effect, the size and strength of the two vortices adjacent to the trailing surface increases while that of the other two vortices adjacent to the leading surface decreases; and 3) vortices on top of ribs shrink in size and get significantly distorted by the Coriolis force only in the region near the top and bottom surfaces. The general effect of the Coriolis-force-induced secondary flow is to distort the rib-induced vortices. Consequently, the temperature contours are shifted toward the trailing surface as shown in the corresponding temperature contour plot in Fig. 8. The heat transfer on all four side surfaces is affected accordingly: divided by plane yz, regions near the trailing side, including the trailing surface and a portion of the top and bottom surfaces adjacent to the trailing surface, have steeper temperature gradient and thus higher heat transfer than the nonrotating case; regions near the leading side, including the leading surface and a portion of the top and bottom surfaces adjacent to the leading surface, have gentler temperature gradient and thus lower heat transfer than the nonrotating case.

Figure 9 shows the cross-stream velocity vectors and temperature contours for the $\beta = 135$ deg case at the same planes as in cases 1 and 2. In the smooth section before the first rib, the Coriolis force produces a distorted cross-stream two-vortex flow structure. The left corner of the vortex near the top surface stretches along the leading surface all of the way to the bottom surface, while the vortex at the bottom shrinks into the corner between the trailing surface and the bottom surface. This Coriolis-force-induced secondary flow pushes the cold fluid away from the corner between the leading and bottom surfaces towards the corner between the trailing and top surfaces. A comparison between Figs. 7 and 9 shows the following:

1) Because of the Coriolis force effect, the size and strength of the rib-induced vortex adjacent to the top-trailing corner increases, and this vortex predominates the top half of the cross section; the size and strength of the rib-induced vortex adjacent to the bottom-trailing

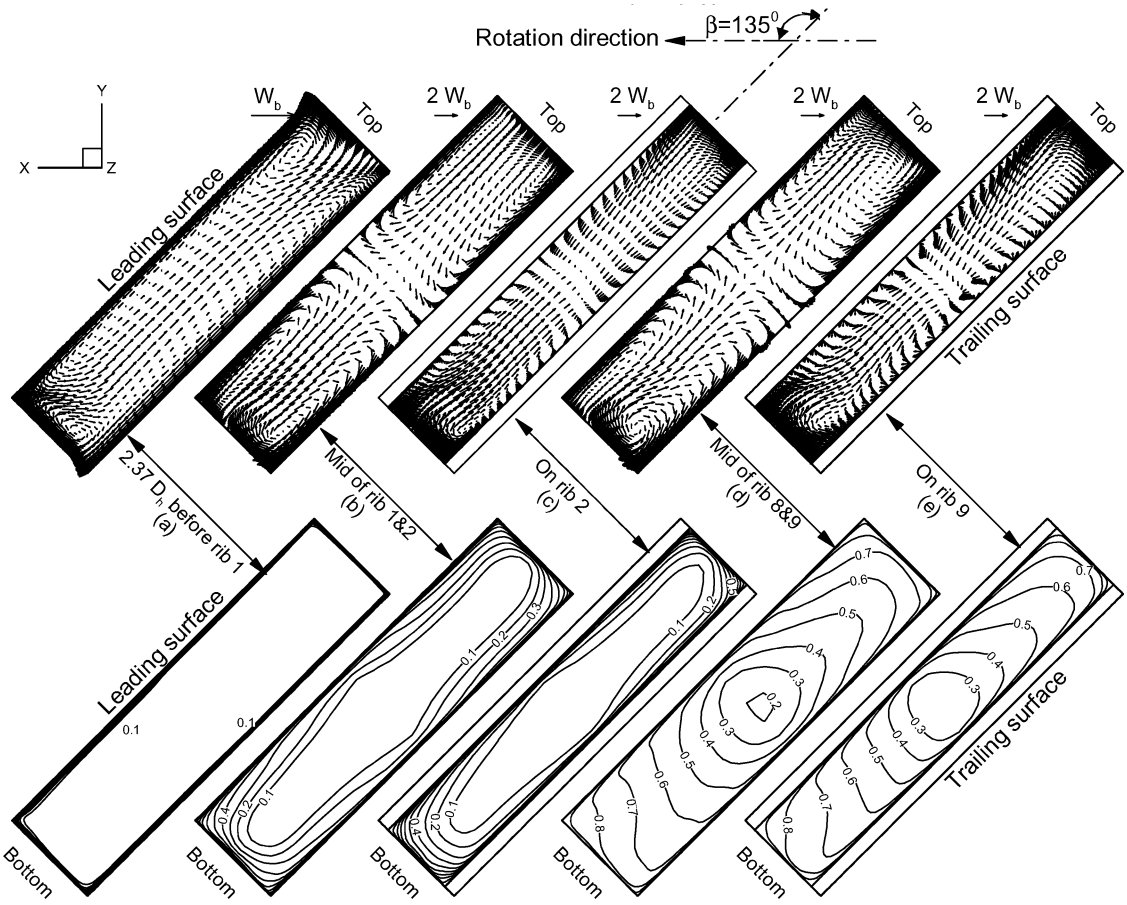

Fig. 9 Secondary flow and dimensionless temperature θ contours for rotating duct ($Re = 10^4$, $\Delta\rho/\rho = 0.122$, $Ro = 0.14$, $\beta = 135$ deg).

corner increase and dominate the triangular region in the bottom-trailing corner of the cross section.

2) Vortices on top of ribs shrink in size and are significantly distorted by the Coriolis force only in the region near the top and bottom surfaces.

3) A net upward fluid motion from the bottom to the top is observed in the core region of the channel.

The net effect of the secondary flowfield is to push the cooler fluid towards the top surface, as illustrated by the temperature contours shown in Fig. 9. Compared to cases 1 and 2, case 3 has steeper temperature gradient on both the top and trailing surfaces and thus higher heat-transfer coefficients in this area.

Heat-Transfer Coefficient Distribution

Effect of Rotation and Channel Orientation on Heat-Transfer Coefficient Distribution

Figure 10 gives the local Nusselt-number ratio contours on the ribbed leading and trailing surfaces for cases 1, 2, 3, and 4, respectively. The nonrotating case in Figs. 10a and 10b is used as a baseline for comparison and discussion. The entrance and exit regions are cut to focus on the ribbed heated section. Figures 10a and 10b show that the Nusselt-number ratio distribution is the same on both the leading and trailing surfaces for the nonrotating case. Highest Nusselt-number ratios are located near the tip of the V-shaped ribs, whereas lowest Nusselt-number ratios are located right before and after the ribs as well as near the top and bottom surfaces. The Nusselt-number ratios between any two ribs are higher in the central area and decrease along the inclined ribs. The high-Nusselt-number region behind the ribs grows from a small heart shape behind the first several ribs to a V shape with two long wings as the coolant flows along in the duct and the rib-induced secondary flow develops.

In the three rotating cases shown in Figs. 10c–10h, the rotation number is 0.14 while the density ratio is kept at 0.122. Overall, compared to the nonrotating case it is quite clear that channel rotation leads to a significant decrease in the Nusselt-number ratios on the leading surface. Rotation pushes the cooler fluid away from the leading surface. Therefore, unlike what happens in the nonrotating case, the heart-shaped high-Nusselt-number regions behind the first several ribs are somewhat restrained from developing into V-shaped high-Nusselt-number regions. On the other hand, the Nusselt-number ratios on the trailing surface increase as a result of channel rotation. The regions of high-Nusselt-number ratio on the trailing surface spread further toward the side walls as compared to the nonrotating case. This is because of the rotation-induced secondary flow that pushes the cooler fluid towards the trailing surface and the side walls adjacent to the trailing surface.

The effect of orientation on Nusselt-number ratios can be seen by comparing the three rotating cases shown in Figs. 10c–10h. Rotation with a channel orientation of 90 deg, as shown in Figs. 10c and 10d, decreases the Nusselt-number ratios on the leading surface and increases the Nusselt-number ratios on the trailing surface, and the Nusselt-number ratio distributions on both surfaces are symmetric along the centerline of the duct. However, rotation with a channel orientation of 135 deg, as shown in Figs. 10e and 10f, pushes the cooler fluid away from the corner between the leading surface and the bottom surface towards the corner between the trailing surface and the top surface. Therefore, the high-Nusselt-number regions, especially the four regions between the first five ribs, on both the leading and trailing surfaces are asymmetric and shifted towards the side walls. Similarly, rotation with a channel orientation of -135 deg, as shown in Figs. 10g and 10h, pushes the cooler fluid away from the corner between the trailing surface and the top surface towards the corner between the leading surface and the bottom surface. Thus, the high-Nusselt-number regions on both the leading and trailing surfaces are also asymmetric and shifted towards the side walls.

Figure 11 presents the spanwise Nusselt-number ratios for the nonrotating case 1 and the rotating case 4 ($\beta = -135$ deg). In

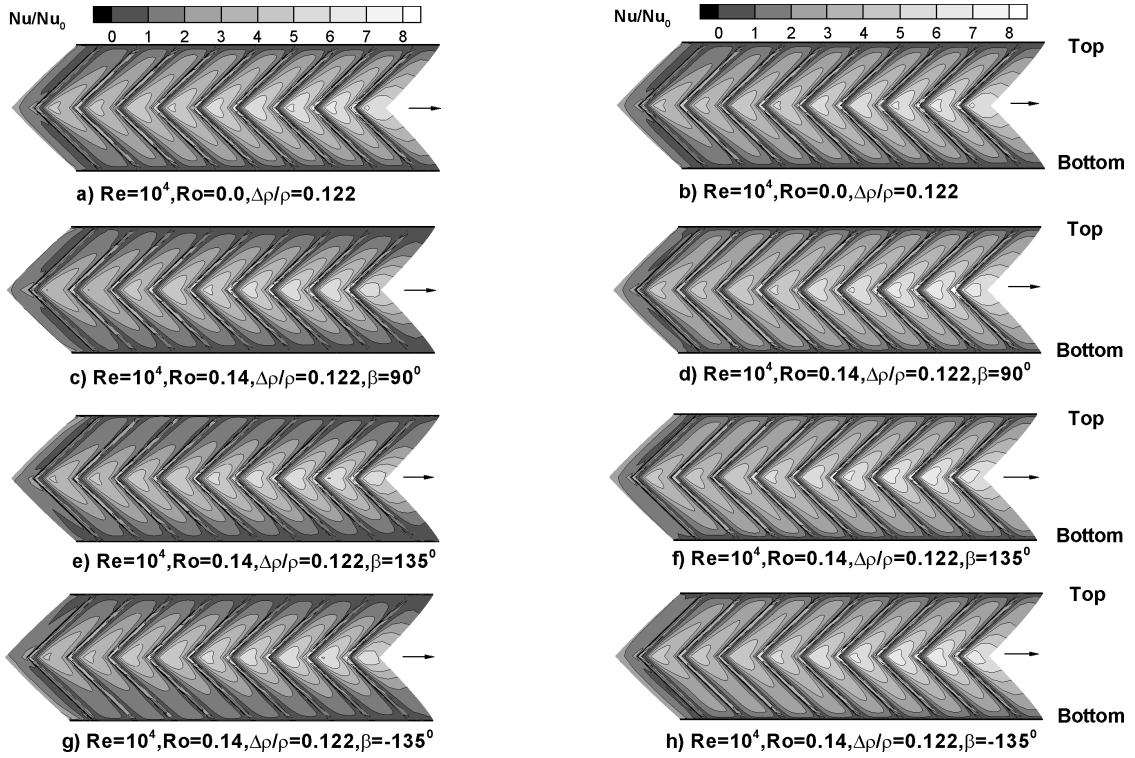

Fig. 10 Nusselt-number ratio contours on leading (a, c, e, g) and trailing (b, d, f, h) surface for lower Reynolds-number ($Re = 10^4$) cases.

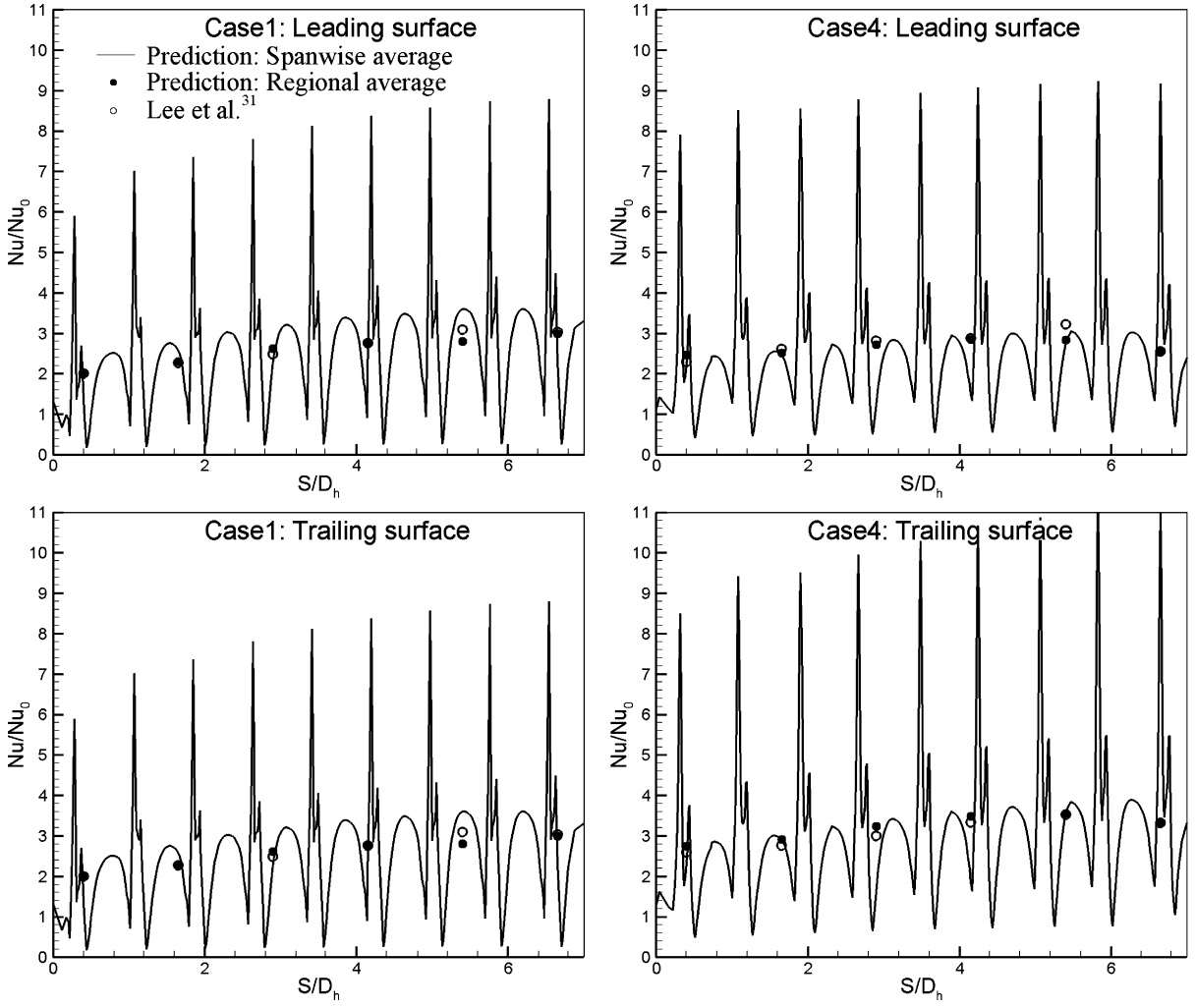

Fig. 11 Comparison between calculated and measured Nusselt-number ratios for nonrotating (case 1) and rotating (case 4: $Ro = 0.14$, $\beta = -135$ deg) ribbed ducts ($Re = 10^4$, $\Delta\rho/\rho = 0.122$).

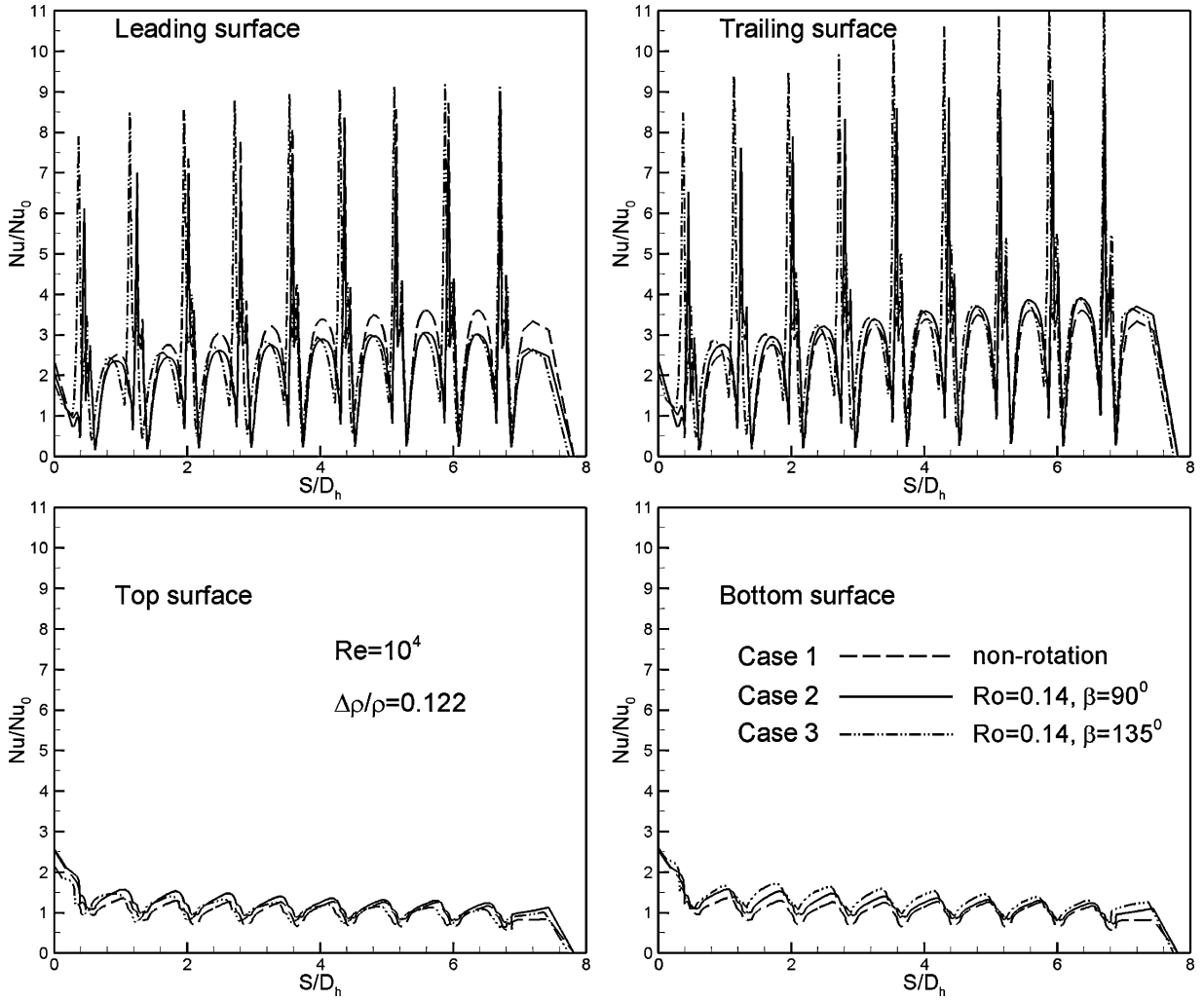

Fig. 12 Effect of rotation and channel orientation on spanwise-averaged Nusselt-number ratios for lower-Reynolds-number ($Re = 10^4$) cases.

addition, regionally averaged Nusselt-number ratios are also presented in Fig. 11 to facilitate a direct comparison with the experimental data of Lee et al.[31] for the same test conditions. It is clearly seen that the numerical predictions for both the nonrotating and rotating cases are in very good agreement with the corresponding measurements. For the nonrotating case, the average discrepancy between the predicted and measured Nusselt-number ratios is only about 3.0%. A similar level of agreement was also observed for the rotating case with an average discrepancy of 4.2%. These results clearly illustrated the capability of the present second-moment RANS method for accurate prediction of the flow and heat-transfer characteristics induced by the V-shaped ribs.

Figure 12 compares the numerically predicted spanwise-averaged Nusselt-number ratios of case 2 ($\beta = 90$ deg) and case 3 ($\beta = 135$ deg) with those of the nonrotating case. In all cases shown in Figs. 11 and 12, the spanwise-averaged Nusselt-number distributions on both the leading and trailing surfaces show periodic spikes. The higher spikes that occur on the rib tops are caused by flow impingement on the ribs; the lower and rounded spikes are caused by flow reattachment between ribs. The Nusselt-number ratios reach a peak value around the eighth rib, indicating a continuously growing rib-induced secondary flow along the duct.

As noted earlier, channel rotation leads to an increase in Nusselt number on the trailing surface and a decrease in Nusselt-number on the leading surface. The Nusselt-number ratios also increase on the top and bottom surfaces as a result of the secondary flow impingement on the side walls. The change of channel orientation from $\beta = 90$ to 135 deg leads to an increase of the spanwise-averaged Nusselt-number ratios on the bottom surface and a minor decrease of the spanwise-averaged Nusselt-number ratios on the top surface, but it has negligible effects on the magnitude of the spanwise-averaged Nusselt-number ratios on both the leading and trailing surfaces. For the $\beta = 135$ deg case, the coolant was pushed towards the corner between the trailing and top surfaces and thus slightly shifts those high Nusselt-number regions towards the upstream direction. This leads to a forward displacement of the spanwise-averaged Nusselt-number ratio curves on all four walls. However, the overall rotation effects are quite small at $Ro = 0.14$ when compared to the heat-transfer enhancement caused by the rib-induced flows.

Effect of High Reynolds Number on Heat-Transfer Coefficient Distribution

Because of the limitation of experimental facility, Lee et al.[31] did not investigate the high-Reynolds-number ($Re \sim 5 \times 10^5$) and high-density-ratio ($\Delta\rho/\rho \sim 0.4$) conditions that could be applied for the blade coolant passage designs of the large power-generation turbines. After successful validations with the experimental data of Lee et al.[31] at low-Reynolds-number and low-density-ratio conditions, it is desirable to extend the present second-moment RANS method for turbine blade cooling applications involving high-Reynolds-number and high-density-ratio and high-rotation-number conditions listed in Table 1 (i.e., cases 5–8). In these calculations, the Reynolds number was increased from 10^4 to 10^5 and 5×10^5, the rotation number was doubled from 0.14 to 0.28, and the density ratio was increased from 0.122 to 0.2 and 0.4. This enables us to evaluate the heat-transfer enhancement in blade coolant passages under more realistic turbine operating conditions.

Figure 13 shows the detailed Nusselt-number ratio contours of the ribbed leading and trailing surfaces for high-Reynolds-number

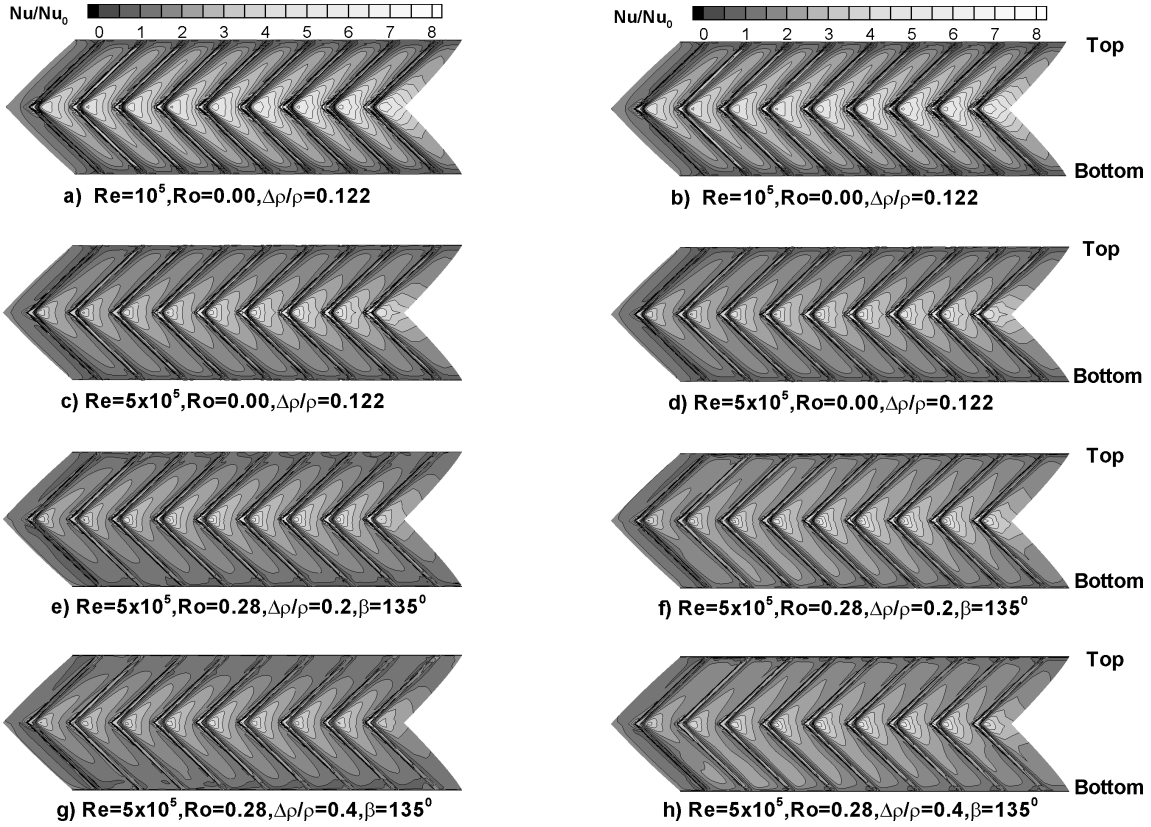

Fig. 13 Nusselt-number ratio contours on leading (a, c, e, g) and trailing (b, d, f, h) surface for high-Reynolds-number cases.

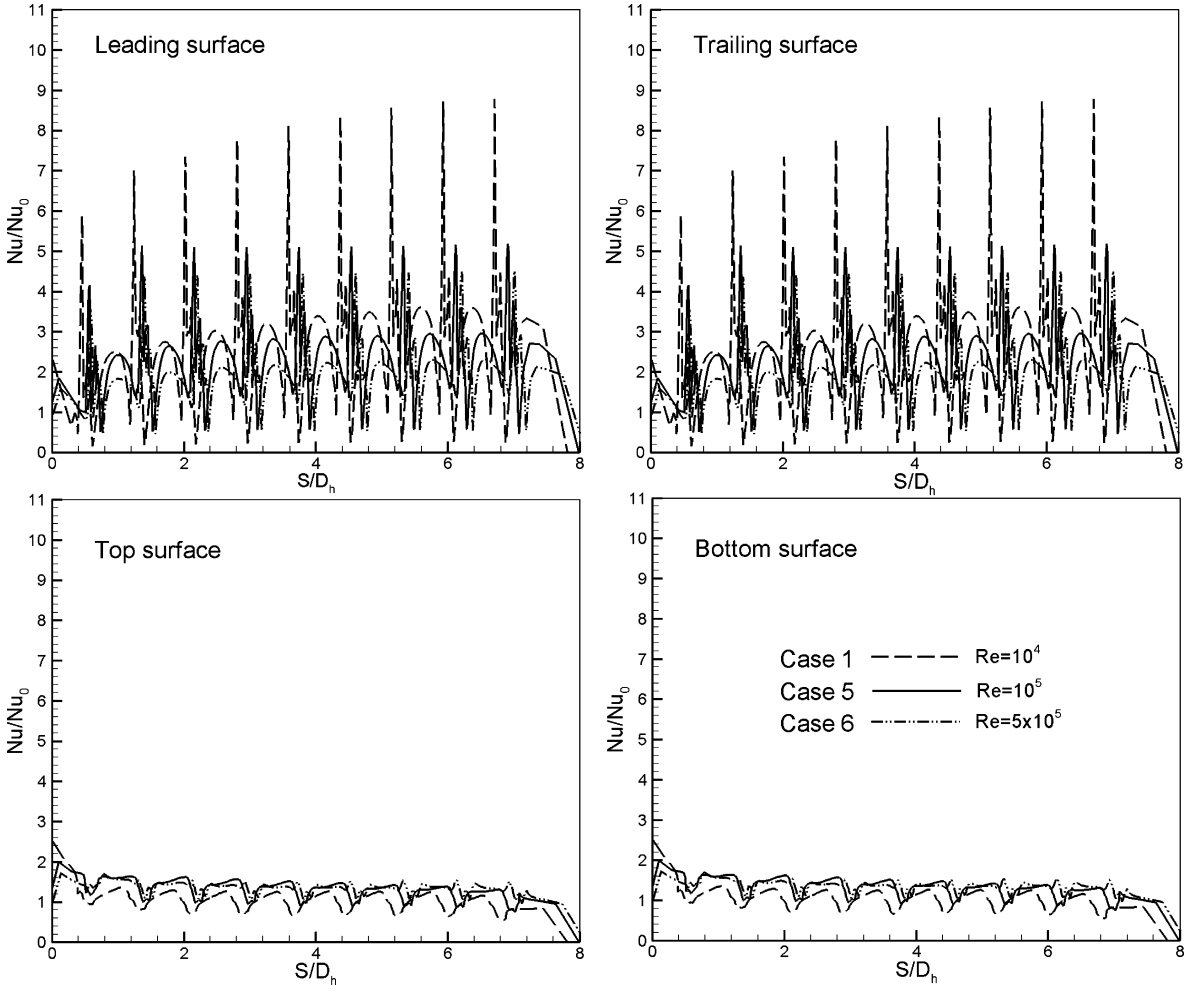

Fig. 14 Effect of Reynolds number on spanwise-averaged Nusselt-number ratios for nonrotating duct ($Ro = 0.0$, $\Delta\rho/\rho = 0.122$).

cases. The entrance and exit regions are cut to focus on the ribbed heated region. For the nonrotating cases shown in Figs. 13a–13d, the highest Nusselt-number ratios are located near the tip of the V-shaped ribs, and the lower Nusselt-number ratios are obtained right before and after the ribs. Between any two ribs, the Nusselt-number ratios near the center are the highest and decrease along the direction of the inclined ribs. When the Reynolds number was increased from 10^4 (case 1) to 10^5 (case 5) and 5×10^5 (case 6), the Nusselt-number ratio in the middle section of the channel decreases significantly, indicating that the heat-transfer enhancement caused by the rib-induced secondary flow is reduced when the thermal boundary layer becomes thinner at high Reynolds numbers.

Figure 14 gives the spanwise-averaged Nusselt-number ratios for the nonrotating duct at three different Reynolds numbers of 10^4, 10^5, and 5×10^5. In general, the Nusselt-number ratios on the leading and trailing surfaces decrease as the Reynolds number increases. On the other hand, the Nusselt-number ratios on the top and bottom surfaces increase with the Reynolds number. However, the actual Nusselt numbers are much higher for the high-Reynolds-number cases because the Nu_0 for smooth duct (proportional to $Re^{0.8}$) is already very high in these cases because of high turbulence and high-temperature gradient inside the boundary layer.

Effect of Rotation and Density Ratio on Heat-Transfer Coefficient Distribution

A comparison between Figs. 13c and 13d, the high-Reynolds-number nonrotating case, and Figs. 13e and 13f, the high-Reynolds-number and high-rotation-number case, shows that channel rotation leads to a significant decrease in Nusselt-number ratio on the leading surface. On the other hand, the Nusselt-number ratios on the trailing surface increase slightly because of the effect of channel rotation. The high Nusselt-number ratio regions on the trailing surface spread toward the side walls. This is because of the rotation-induced secondary flow that pushes the cooler fluid towards the trailing surface and side walls. In cases shown in Figs. 13e–13h, the density ratio is increased from 0.20 to 0.40, while the Reynolds number and rotation number are kept the same. It is quite clear that an increase in density ratio leads the Nusselt-number ratios to further decrease on the leading surface and slightly decrease on the trailing surface. This is because an increased density ratio intensifies the effect of the rotation-induced Coriolis force.

Figure 15 compares the spanwise-averaged Nusselt-number ratios of case 6 with those of cases 7 and 8. Case 7 has a density ratio of 0.2, and case 8 has a density ratio of 0.4. As noted earlier, channel rotation leads to an increase in Nusselt number on the trailing surface and a decrease in Nusselt number on the leading surface. At a rotation number of 0.28, an increase in density ratio (from $\Delta\rho/\rho = 0.2$ to $\Delta\rho/\rho = 0.4$) reduces the heat-transfer coefficients on both the leading and trailing surfaces. In general, a change in density ratio does not have an obvious effect on the Nusselt-number ratios on the leading and trailing surfaces until the flow reaches about halfway of the heated channel section. The combination of rotation and higher density ratio has a net effect of reducing the Nusselt-number ratios on the leading surface. The effects of rotation and higher density ratio tend to offset each other on the trailing surface, but the total effect is still to increase the Nusselt-number ratios on the trailing surface. As the density ratio increases from 0.2 to 0.4, significant enhancements in Nusselt-number ratios are observed on the top and bottom surfaces.

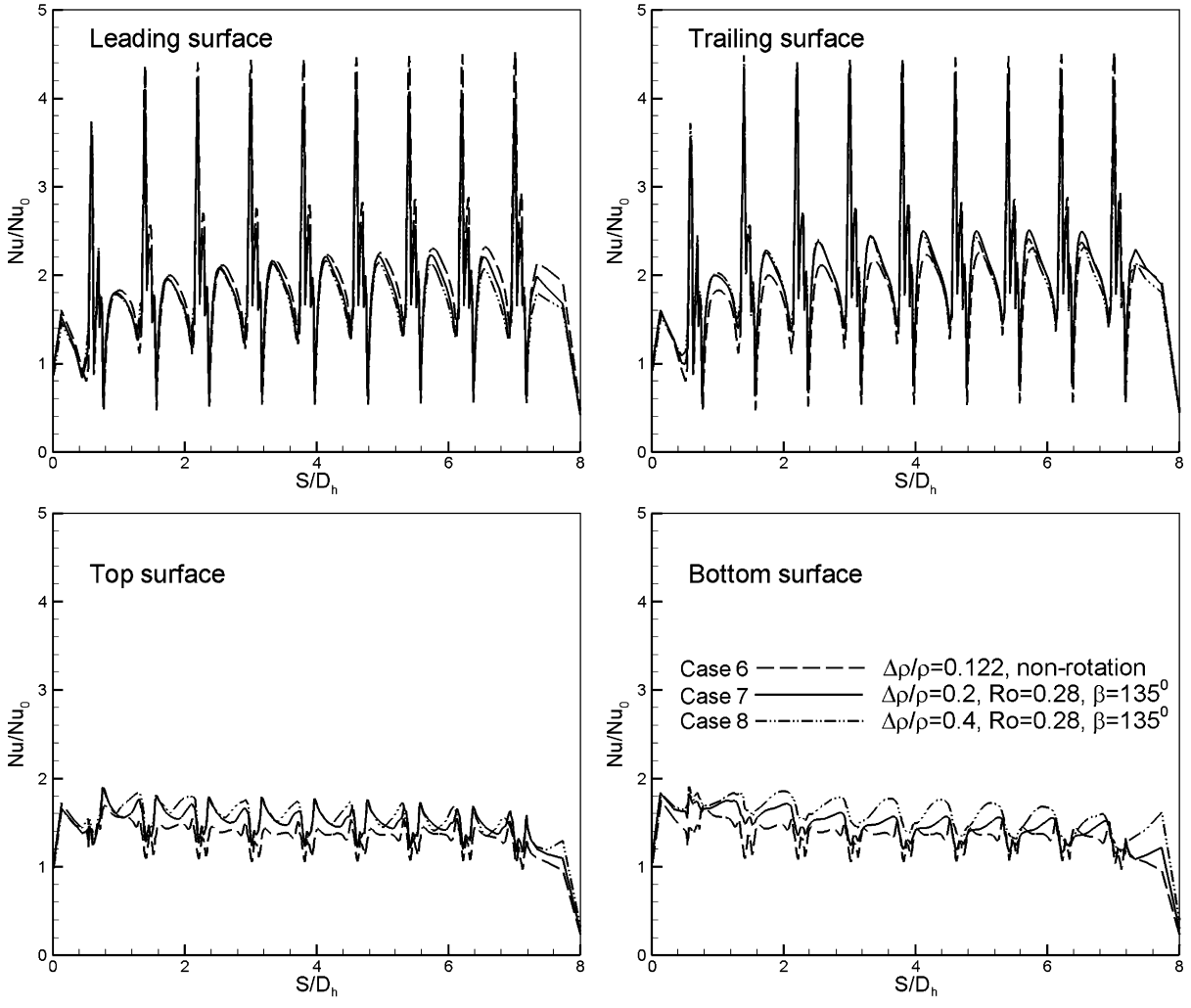

Fig. 15 Effect of rotation and density ratio on spanwise-averaged Nusselt-number ratios for high Reynolds number ($Re = 5 \times 10^5$) cases.

Conclusions

A multiblock Reynolds-averaged Navier–Stokes method was employed to predict three-dimensional flow and heat transfer in a rotating rectangular channel with V-shaped ribs and an aspect ratio of 4:1. It predicted fairly well the complex three-dimensional flow and heat-transfer characteristics resulting from the large channel aspect ratio, rotation, centrifugal buoyancy forces, and channel orientation. Main findings from this study are summarized as follows:

1) The Nusselt-number ratios predicted by the present near-wall second-moment closure model are in very good agreement with the experimental data for both the nonrotating and rotating cases.

2) The V-shaped ribs induce four counter-rotating vortices that oscillate in size along the streamwise direction. For the nonrotating case, the secondary flow results in steep temperature gradients and high heat-transfer coefficients on the surfaces with V-shaped ribs as well as side walls.

3) For rotating cases, the rotation-induced cross-stream secondary flow distorts the V-shaped rib-induced vortices and affects the heat transfer on both the leading and trailing surfaces.

4) The V-shaped ribs create a symmetric heat-transfer enhancement from the channel centerline towards the sidewalls. The rotation increases heat-transfer enhancement on the trailing surface and decreases heat-transfer enhancement on the leading surface.

5) The $\beta = 90$ deg rotation creates a symmetric heat-transfer distribution. However, the $\beta = 135$ and -135 deg channel orientations generate asymmetric heat-transfer distributions from the channel centerline to the side walls.

6) High Reynolds numbers tend to weaken the heat-transfer enhancement effect of the V-shaped rib-induced secondary flow.

7) For high-Reynolds-number cases, an increase in rotation number and density ratio leads the Nusselt-number ratios on the leading surface to further decrease, the Nusselt-number ratios on the trailing surface to increase first (case 7) and then slightly decrease (case 8), and the Nusselt-number ratios on the side walls to further increase.

Acknowledgment

This publication was prepared with the support of the U.S. Department of Energy (DOE), Office of Fossil Energy, and National Energy Technology Laboratory. However, any opinions, findings, conclusions, or recommendations expressed herein are those of the authors and do not necessarily reflect the views of the DOE. The computations were performed on the SGI Origin 3800 at the Texas A&M Supercomputer Center under a supercomputer research grant. The support of all of the preceding institutions is greatly appreciated.

References

[1] Stephens, M. A., Shih, T. I.-P., and Civinskas, K. C., "Computation of Flow and Heat Transfer in a Rectangular Channel with Ribs," AIAA Paper 95-0180, Jan. 1995.

[2] Stephens, M. A., Chyu, M. K., and Shih, T. I.-P., "Computation of Convective Heat Transfer in a Square Duct with Inclined Ribs of Rounded Cross Section," American Society of Mechanical Engineers, Paper 96-WA/HT-12, Nov. 1996.

[3] Lin, Y.-L., Shih, T. I.-P., Stephens, M. A., and Chyu, M. K., "A Numerical Study of Flow and Heat Transfer in a Smooth and a Ribbed U-Duct with and Without Rotation," *Journal of Heat Transfer*, Vol. 123, No. 2, 2001, pp. 219–232.

[4] Prakash, C., and Zerkle, R., "Prediction of Turbulent Flow and Heat Transfer in a Ribbed Rectangular Duct with and Without Rotation," *Journal of Turbomachinery*, Vol. 177, No. 2, 1995, pp. 255–264.

[5] Bonhoff, B., Tomm, U., Johnson, B. V., and Jennions, I., "Heat Transfer Predictions For Rotating U-Shaped Coolant Channels with Skewed Ribs and with Smooth Walls," American Society of Mechanical Engineers, Paper 97-GT-162, June 1997.

[6] Iacovides, H., "Computation of Flow and Heat Transfer Through Rotating Ribbed Passage," *International Journal of Heat and Fluid Flow*, Vol. 19, No. 5, 1998, pp. 393–400.

[7] Chen, H. C., Jang, Y. J., and Han, J. C., "Computation of Heat Transfer in Rotating Two-Pass Square Channels by a Second-Moment Closure Model," *International Journal of Heat and Mass Transfer*, Vol. 43, No. 9, 2000, pp. 1603–1616.

[8] Chen, H. C., Jang, Y. J., and Han, J. C., "Near-Wall Second-Moment Closure for Rotating Multi-Pass Cooling Channels," *Journal of Thermophysics and Heat Transfer*, Vol. 14, No. 2, 2000, pp. 201–209.

[9] Jang, Y. J., Chen, H. C., and Han, J. C., "Computation of Flow and Heat Transfer in Two-Pass Channels with 60° Ribs," *Journal of Heat Transfer*, Vol. 123, No. 3, 2001, pp. 563–575.

[10] Jang, Y. J., Chen, H. C., and Han, J. C., "Numerical Prediction of the Flow and Heat Transfer in a Two-Pass Square Duct with 90° Ribs," *International Journal of Rotating Machinery*, Vol. 7, No. 3, 2001, pp. 195–208.

[11] Ekkad, S. V., and Han, J. C., "Detailed Heat Transfer Distributions in Two-Pass Square Channels with Rib Turbulators," *International Journal of Heat and Mass Transfer*, Vol. 40, No. 11, 1997, pp. 2525–2537.

[12] Jang, Y. J., Chen, H. C., and Han, J. C., "Flow and Heat Transfer in a Rotating Square Channel with 45° Angled Ribs by Reynolds Stress Turbulence Model," *Journal of Turbomachinery*, Vol. 123, No. 1, 2001, pp. 124–132.

[13] Johnson, B. V., Wagner, J. H., Steuber, G. D., and Yeh, F. C., "Heat Transfer in Rotating Serpentine Passage with Trips Skewed to the Flow," *Journal of Turbomachinery*, Vol. 116, No. 1, 1994, pp. 113–123.

[14] Al-Qahtani, M. S., Jang, Y. J., Chen, H. C., and Han, J. C., "Prediction of Flow and Heat Transfer in Rotating Two-Pass Rectangular Channels with 45° Rib Turbulators," *Journal of Turbomachinery*, Vol. 124, No. 2, 2002, pp. 242–250.

[15] Azad, G. S., Uddin, M. J., Han, J. C., Moon, H. K., and Glezer, B., "Heat Transfer in a Two-Pass Rectangular Rotating Channel with 45° Angled Rib Turbulators," *Journal of Turbomachinery*, Vol. 124, No. 2, 2002, pp. 251–259.

[16] Al-Qahtani, M. S., Chen, H. C., and Han, J. C., "A Numerical Study of Flow and Heat Transfer in Rotating Rectangular Channels ($AR = 4$) with 45° Rib Turbulators by Reynolds Stress Turbulence Model," *Journal of Heat Transfer*, Vol. 125, No. 1, 2003, pp. 19–26.

[17] Griffith, T. S., Al-Hadhrami, L., and Han, J. C., "Heat Transfer in Rotating Rectangular Cooling Channels ($AR = 4$) with Angled Ribs," *Journal of Heat Transfer*, Vol. 124, No. 3, 2002, pp. 617–625.

[18] Jia, R., Saidi, A., and Sunden, B., "Heat Transfer Enhancement in Square Ducts with V-Shaped Ribs of Various Angles," American Society of Mechanical Engineers, Paper GT-2002-30209, June 2002.

[19] Han, J. C., and Park, J. S., "Developing Heat Transfer in Rectangular Channel with Rib Turbulators," *International Journal of Heat and Mass Transfer*, Vol. 31, No. 1, 1988, pp. 183–195.

[20] Han, J. C., Zhang, Y. M., and Lee, C. P., "Augmented Heat Transfer in Square Channels with Parallel, Crossed, and V-Shaped Angled Ribs," *Journal of Heat Transfer*, Vol. 113, No. 3, 1991, pp. 590–596.

[21] Liou, T.-M., Tzeng, Y.-Y., and Chen, C.-C., "Fluid Flow in a 180 Deg Sharp Turning Duct with Different Divider Thicknesses," American Society of Mechanical Engineers, Paper 98-GT-189, Jan. 1998.

[22] Wagner, J. H., Johnson, B. V., and Kopper, F. C., "Heat Transfer in Rotating Serpentine Passage with Smooth Walls," *Journal of Turbomachinery*, Vol. 113, No. 3, 1991, pp. 321–330.

[23] Dutta, S., and Han, J. C., "Local Heat Transfer in Rotating Smooth and Ribbed Two-Pass Square Channels with Three Channel Orientations," *Journal of Heat Transfer*, Vol. 118, No. 3, 1996, pp. 578–584.

[24] Soong, C. Y., Lin, S. T., and Hwang, G. J., "An Experimental Study of Convective Heat Transfer in Radially Rotating Rectangular Ducts," *Journal of Heat Transfer*, Vol. 113, No. 3, 1991, pp. 604–611.

[25] Wagner, J. H., Johnson, B. V., Graziani, R. A., and Yeh, F. C., "Heat Transfer in Rotating Serpentine Passages with Trips Normal to the Flow," *Journal of Turbomachinery*, Vol. 114, No. 4, 1992, pp. 847–857.

[26] Johnson, B. V., Wagner, J. H., Steuber, G. D., and Yeh, F. C., "Heat Transfer in Rotating Serpentine Passage with Selected Model Orientations for Smooth or Skewed Trip Walls," *Journal of Turbomachinery*, Vol. 116, No. 4, 1994, pp. 738–744.

[27] Parsons, J. A., Han, J. C., and Zhang, Y. M., "Effects of Model Orientation and Wall Heating Condition on Local Heat Transfer in a Rotating Two-Pass Square Channel with Rib Turbulators," *International Journal of Heat and Mass Transfer*, Vol. 38, No. 7, 1995, pp. 1151–1159.

[28] Zhang, Y. M., Han, J. C., Parsons, J. A., and Lee, C. P., "Surface Heating Effect on Local Heat Transfer in a Rotating Two-Pass Square Channel with 60-deg Angled Rib Turbulators," *Journal of Turbomachinery*, Vol. 117, No. 2, 1995, pp. 272–280.

[29] Al-Hadhrami, L., and Han, J. C., "Effect of Rotation in Two-Pass Square Channels with Five Different Orientations of 45° Angled Rib Turbulators," *International Journal of Heat and Mass Transfer*, Vol. 46, No. 5, 2003, pp. 653–669.

[30] Al-Hadhrami, L., Griffith, T. S., and Han, J. C., "Heat Transfer in Two-Pass Rotating Rectangular Channels ($AR = 2$) with Five Different Orientations of 45° V-shaped Rib Turbulators," *Journal of Heat Transfer*, Vol. 125, No. 2, 2003, pp. 232–242.

[31] Lee, E., Wright, L. M., and Han, J. C., "Heat Transfer in Rotating Rectangular Channels ($AR = 4{:}1$) with V-Shaped and Angled Rib Turbulators with and Without Gaps," American Society of Mechanical Engineers, Paper GT-2003-38900, June 2003.

[32] GRIDGEN User Manual, ver. 13.3, Pointwise, Inc., Bedford, TX, 1999.